Li *et al. J Wireless Com Network* (2022) 2022:106
https://doi.org/10.1186/s13638-022-02172-w

EURASIP Journal on Wireless Communications and Networking

RESEARCH Open Access

Integrated sensing and communication in 6G: a prototype of high resolution multichannel THz sensing on portable device

Oupeng Li[1], Jia He[1], Kun Zeng[1], Ziming Yu[1], Xianfeng Du[1], Zhi Zhou[1*], Yuan Liang[1], Guangjian Wang[1], Yan Chen[2], Peiying Zhu[2], Wen Tong[2], David Lister[3] and Luke Ibbetson[3]

*Correspondence: zhouzhi19@huawei.com

[1] Huawei Technologies Co., Ltd., Chengdu, China
[2] Huawei Technologies Canada Co., Ltd., Ottawa, Canada
[3] Vodafone Group, Newbury, UK

Abstract

6G is believed to go beyond communication and provide integrated sensing and computing capabilities for a vision of Connected Intelligence with everything connected, everything sensed, and everything intelligent. Integrated sensing and communication will play a vital role for the fusion of physical and cyber worlds. The exploration of higher frequency bands, larger bandwidth, and more advanced large antenna technologies is paving the way towards the goal. In particular, the study of THz opens the possibility to have high resolution sensing and imaging capability on a communication mobile device. In this paper, we take a step along this direction and justify such possibility by building a THz sensing prototype with millimeter level imaging resolution while considering the physical aperture constraint of typical mobile device.

Keywords: Integrated Sensing and Communication (ISAC), 6G, THz sensing, THz imaging, Portable imaging

1 Introduction

Every 10 years, there will be a new generation upgrade of mobile communications. As we witness the global roll-out of 5G wireless networks in 2020, we are seeing the emerging of 6G around horizon 2030. However, the major paradigm shifts take two generations to mature, e.g. from voice to mobile internet, from connected people to connected everything. 6G is the next-generation mobile communications system, but it will go far beyond communications. We believe 6G is to open a new era of Connected Intelligence to meet the human and societal challenges in many fronts. In particular, 6G will serve as a distributed neural network that provides sensing, communication and computing capabilities to fuse the physical, cyber, and biological worlds, truly ushering in an era in which everything will be sensed, connected, and intelligent.

In particular, thanks to the increased number of antennas and wider bandwidth at higher frequency band (e.g. up to THz), sensing will become a natively supported function and key enabler in 6G systems. The communications system as a whole can serve a sensor. It can explore the radio wave transmission, echo, reflection, and scattering to

sense and better understand the physical world. The integration of the sensing and communication will enable many new services which the cellular operators can offer such as better transportation management, better positioning service and public safety. It also helps improve wireless communication networks (with the help of AI) which will be tailored to the gathered environment information. The integration of sensing and communication (ISAC) can happen at different levels, from loosely co-located [1, 2] to totally integrated. The sharing between the two systems can start from spectrum, hardware, to more advanced signal processing, or even cross-module, cross-layer protocol design, benefiting each other. The possible applications of ISAC could include but not limited to serving as assistive technologies for visually impaired people, working for game/motion-sensors with connection to gaming console, enabling health and well-being support, driving support with vehicle-to-vehicle sensing and communications, head movement tracking support on XR devices, and gesture recognition support to control your smartphone in a touchless way with sequences of finger movements patterns.

The operating bandwidth for each mobile communication generation follows five times and more rules as shown in Fig. 1. While low bands remain the most cost-effective way for wide coverage, the millimeter wave bands become mature in the 5G and 6G due to new drivers such as sensing. On the other hand, recent development in semiconductor technology has bridged the "THz band gap", which is expected to stimulate various THz sensing applications such as ultra-high resolution imaging and molecular level spectrogram analysis. The ultra-wide bandwidth in THz will also enable Tbps data rate transmission especially in short-range communications. And also open new possibilities for high resolution sensing. ISAC system design with THz band has thus become an attractive research area.

Also, standardization and regulation study of the THz bands are now ongoing [3]. For a long time, THz spectrum are described as the last virgin land of the radio spectrum. Only a few scientific and astronomical services are deployed in these frequency bands, especially the bands above 275 GHz, for the practical technical limitations, in spite of there are abundant spectrum and supporting a high transmission rate, strong anti-interference, and are suitable for meeting the Tbps-level communications. However, this has partially changed with the development of integrated components and circuits, and the emergence of various services that require ultra-high data rate transmission. At the World Radiocommunication Conference 2019 (WRC-19), RR No. 5.564A was approved, and four globally harmonized frequency bands with a total bandwidth of 137 GHz (i.e. 275–296 GHz, 306–313 GHz, 318–333 GHz and 356–450 GHz) are allocated for the

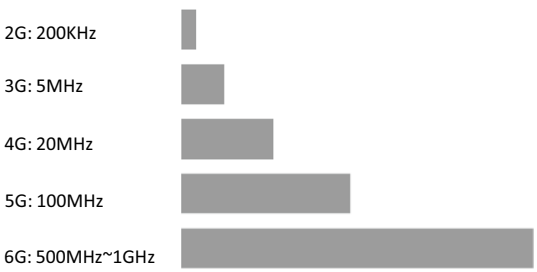

Fig. 1 Operating bandwidth increment in each generation

implementation of land mobile and fixed service application in the frequency range of 275–450 GHz, on the basis of study outcomes of Agenda Item 1.15 (WRC-19). Therefore, with the addition of the spectrum allocated at the previous WRCs, there are more than 230 GHz Mobile Service (MS) spectrum. The allocated mobile frequency bands with a contiguous bandwidth would be greater than 5 GHz.

With the application of THz ISAC design, it is expected to open many opportunities in Fig. 2 for brand new services especially on future mobile devices or even wearables. The purpose of this paper is to take a step forward along the direction of ISAC with THz band, trying to justify the feasibility of providing high resolution (e.g. millimeter level) THz sensing capability on portable communication device. In particular, a prototype is setup for this verification purpose and a solution of virtual aperture is proposed and implemented to solve the conflicting requirements of large aperture size for high sensing resolution and compact device size for its mobile device nature.

The contribution of this paper can be summarized as follows:

- In terms of hardware, this paper demonstrated a portable compact THz prototype with multi-channel integrated transceiver chips and the terahertz communication and sensing capability for the first time in the industry.
- In terms of sensing, this paper evaluated the performance of two typical waveform: FMCW and OFDM. What's more, a noval optimization method based on geometric interpretation for SIMO sparse imaging to accomplish near-real-time cm-level imaging is presented in this paper.

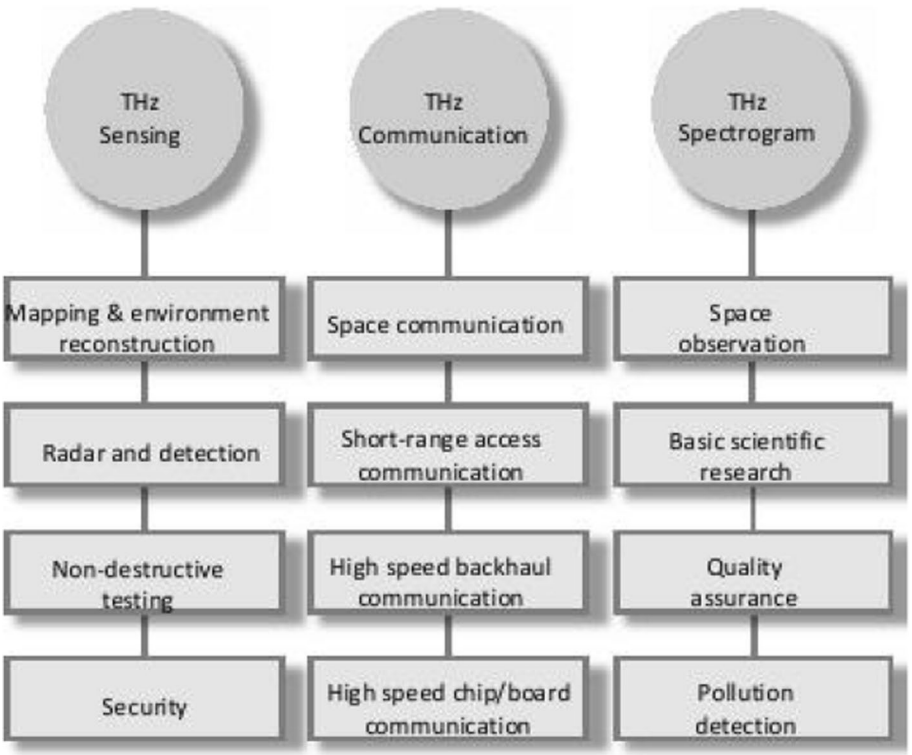

Fig. 2 THz application in sensing and communication

2 ISAC system with THZ band

2.1 Advantageous of THz sensing and potential use cases

With the multi-level vertical cellular network and ubiquitous coverage of cellular systems, sensing can be used to create a detailed live city map, including buildings, cars and pedestrians. This type of map could be used for many smart city services such as virtual city planning with impact studies, on demanding maintenance, traffic control, etc., and autonomous driving cars as in Fig. 3. On the other hand, ISAC portable devices enabled by high frequencies will open the door for numerous applications such as augment human senses. It empowers people to "see" beyond the limits of human eyes with portable, wearable or implanted devices. It facilitates information collection in darkness, inside a box, and beneath the skin with high resolution. Remote surgery, detection of slits on products, and sink leakage detection are prospective scenarios in daily life.

Enabled by ISAC system, we can turn cellular system to a sensor, virtualizing environment, analyzing materials and monitoring status of the person. It is also feasible to build a link between physical, biological and cyber world. With sensing capability, surrounding information can be built inside cyber space, which in turn improve physical and biological world.

THz sensing is preferred due to its ultra-bandwidth and small device size. Furthermore, as the molecular vibration characteristics of the terahertz band, unique spectrogram identification capability is provided [4]. Besides high throughput in communication, THz would facilitate the utility of sensing such as enhanced human senses, postures recognition and industrial localization.

Figure 4a summarized the first order advantages of THz sensing and Fig. 4b gives the high level comparison of THz sensing with other types of sensing. LiDAR stands for Light Detection and Ranging and CT stands for computed tomography. It can be seen that compared with professional CT and LiDAR equipment, THz sensing has advantage in portability, safety, and feasibility to integrate with wireless communication. While compared with centimeter or millimeter wave sensing, THz sensing enjoys clear benefit of much higher resolution and accuracy. Benifit from these advantages, Thz sensing research has long attracted attention. The THz penetration characteristic was studied

Fig. 3 Sensing for live city map

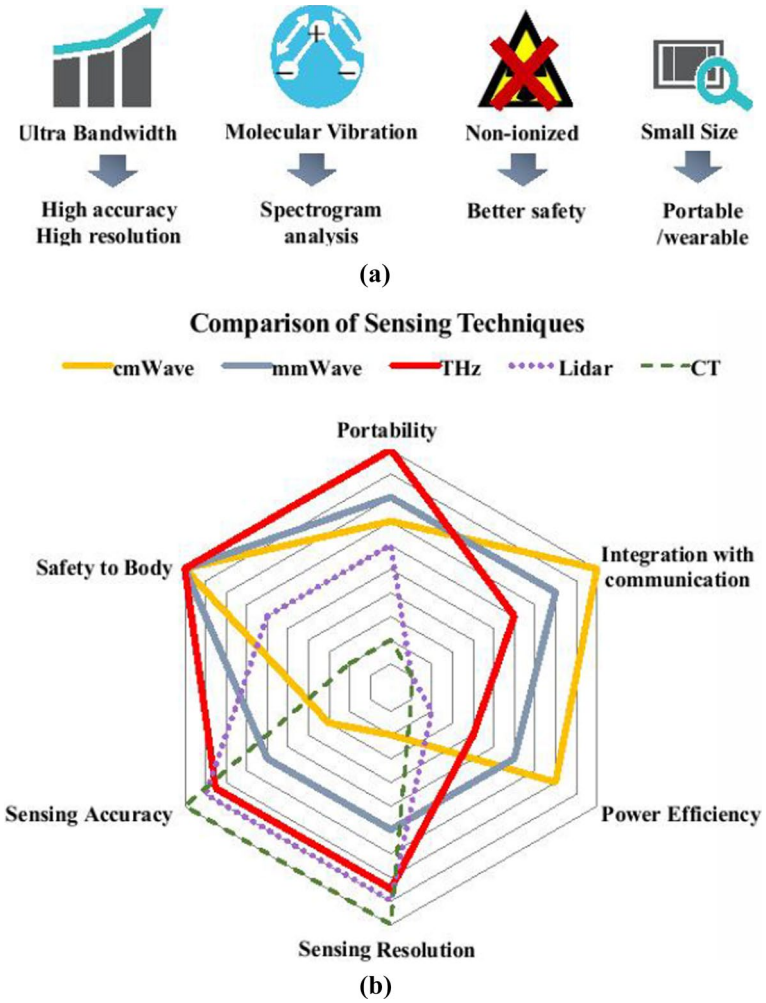

Fig. 4 High level illustration of the features of THz sensing. **a** Advantages of THz sensing. **b** High level comparison of different sensing techniques

in tumor identification [5], which was able to distinguish between normal and tumor tissues without additional damage as X-rays do. Beside the medical appllication, non-destructive detection of THz is also promising in quality control and secuirty scanning [6, 7], With technologies such as virtual aperture and sparse sampling, it is possible to image a distant object with millimeter accurcy.

2.2 Potential challenges in integrated system design

In some sense, wireless sensing can be interpreted as a communication method which conveys information embedded in the communication medium by transmitting a wireless signal, and then receiving and analyzing its reflections [8]. However, compared with communication, sensing is a very different function that has different set of metrics to optimize. Fundamental tradeoffs between communication and sensing in the design and performance characterizing of an ISAC system have thus attracted research investigations [9]. It is desirable to characterize such tradeoffs and identify potential challenges to get better understanding for ISAC system design.

In particular, for a THz ISAC system on portable devices, it is expected that the new sensing applications (such as hidden object imaging) can be performed via THz signals that are used for ultra-high speed communications (such as for short range communications). In this case, the major design challenges come from both hardware design and air interface design.

Firstly, from the aspect of hardware design, there are contradicting requirements for the two functions [10, 11]. For high resolution sensing application, especially high cross-range resolution applications, thousands of antenna elements are required to create large enough aperture for signal detection. However, this is conflicting with the design requirement of a communication device that has strict constraints on the size and power consumption for commercialization. To solve this problem, virtual aperture approaches are applied in our prototype system. In particular, virtual multiple-input multiple-output (MIMO) design in the hardware transceiver architecture and sparse sampling design in the scanning process are proposed and combined.

From the aspect of the air interface design for an ISAC system, on the other than, substantial works have been done on joint waveform design [12]. The main challenge comes from the contradicting key performance indicators (KPIs) in the design, i.e. spectral efficiency for communication, and resolution and accuracy for sensing. The jointly designed waveform enables a signal to support both functions [13]. As a first step, in our prototype design, communication oriented waveform (such as rrthogonal frequency division multiplexing (OFDM)-based waveform) is evaluated and compared with sensing oriented waveform (such as linear frequency modulation (LFM)-based waveform) in terms of range and cross-range accuracy. State of the art study suggests that there is still room for joint waveform design to achieve the best tradeoff between communication capacity and sensing accuracy [12], which will be our next step investigation work.

3 Prototype design for high resolution THZ imaging on portable devices

As aforementioned, the biggest challenge on the hardware design comes from the fact that to support a high-precision sensing resolution, especially in the cross-range domain, a large enough aperture (up to thousands of antenna elements) is required. Given the size and power constraint of a portable device, however, it is clear that physically packing thousands of antenna elements is infeasible.

Therefore, to implement an ISAC system with a simple hardware architecture, i.e. limited number of antenna elements in a practical size with low cost and low power consumption, a solution of virtual aperture with MIMO structure and sparse scanning approach is proposed in this paper.

The virtual aperture is constructed in two steps. In the first step, MIMO structure is implemented in the hardware architecture to form a virtual aperture larger than the physical aperture constructed by the antenna elements, as elaborated; in the second step, a sparse scanning approach is applied, transforming the degree-of-freedom in time and space into larger virtual aperture.

3.1 Hardware architecture

To implement the solution of virtual aperture, the hardware architecture of the proposed ISAC system needs to support the following requirements:

(1) Multiple transciever (TRX) chains to support MIMO structure as the first step for the overall virtual aperture.
(2) Wide antenna pattern to cover the target scanning area to maintain the correlation among the reflected samplings.
(3) Real-time position information (cm-level from MEMS) of the device to perform coherent process of the received signals.

The schematic of the prototype architecture is shown in Fig. 5. The prototype is built to work at 140 GHz carrier frequency with 8 GHz bandwidth. The transmitter antenna array has 4 RF ports while the receiver antenna array has 16 radio frequency (RF) ports, forming a 4T16R MIMO structure. When the transmitter transmits mutually orthogonal signals from 4 transmit antennas, these waveforms can be extracted from each of the 16 receive antennas by a set of matched filters, equivalently forming a virtual array with 64 antenna elements. As mentioned earlier, this is the first step to construct the virtual aperture. An even larger scale virtual array can be equivalently achieved by sparse scanning that will be elaborated in the next subsection, forming a final virtual aperture equivalent to that with thousands of antenna elements. The local oscillator signal is

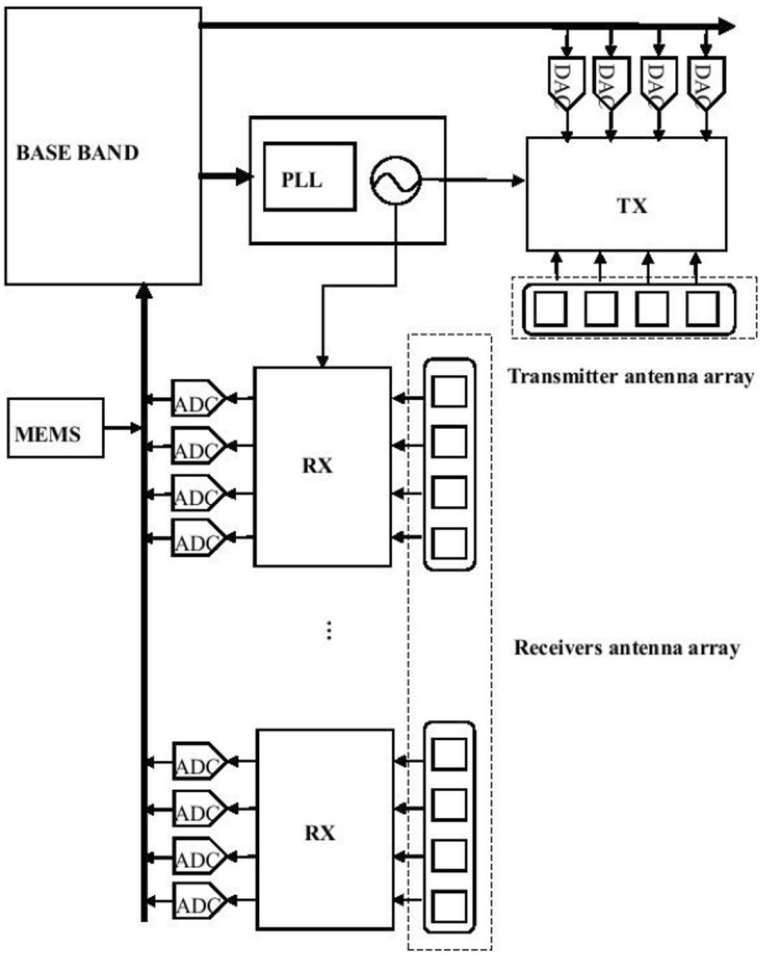

Fig. 5 Illustration of the architecture of ISAC prototype

provided by a phase-locked loop (PLL) controlled by the baseband. The micro-electro-mechanical system (MEMS) gyroscope is used to record the trajectory and posture of the sensing device.

Figure 6 shows the 3 dimensional (3D) model of the Terahertz frond end. The waveguide antenna is fabricated in three part. The transceiver chips are mounted on the substrate unit together with the h-plane probe which converts the signal form micro-strip line to waveguide. The radiation unit is an array of horn antenna, where the antenna elements are sparsely placed with a spacing of 2.14 mm, which is equivalent to the wavelength at 140 GHz.

The antenna radiation unit is a wide beam design with a 3 dB lobe width of 50°, which can cover about 0.9×0.9 m^2 at a distance of one meter. The 3D antenna pattern and gain pattern at phi $= 90^\circ$ are given in Fig. 7. The antenna gain is about 7dBi.

The output power of the transmitter chip is 10 dBm and the receiver noise figure is about 10 dB. Considering about 2 dB transmission loss, the system output effective isotropic radiated power (EIRP) is around 15 dBm. Under such specifications, within 5m distance, a THz ISAC system could support 16 quadrature amplitude modulation (QAM) transmission for communication and at the same time achieve mm-level resolution for sensing and imaging. If only imaging is performed, the maximum imaging distance can be longer. The main reason is that the signal-to-noise ratio can be improved by coherent accumulation during imaging.

3.2 Imaging approach with sparse sampling

In this subsection, we first discuss the implementation issues and challenges in imaging under the hardware architecture and then propose our design considerations and related imaging approach.

The first challenge we encountered is that the number of antennas used for joint communication and sensing on portable devices is limited. For example, there are only 4 transmit antennas and 16 receive antennas for the antenna array. Furthermore, in order to avoid the strong side-lobe interference, the spacing between these antennas should be kept about half a wavelength apart. This will constraint the aperture size of the array

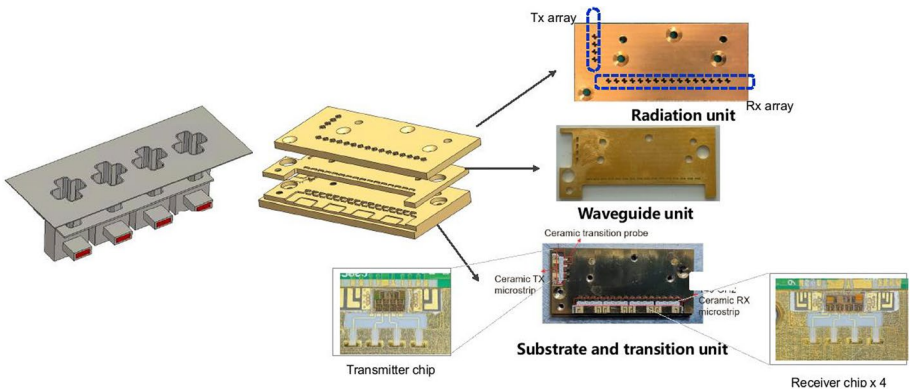

Fig. 6 The 3D structure of microstrip to waveguide transition probe and circular polarization waveguide antenna

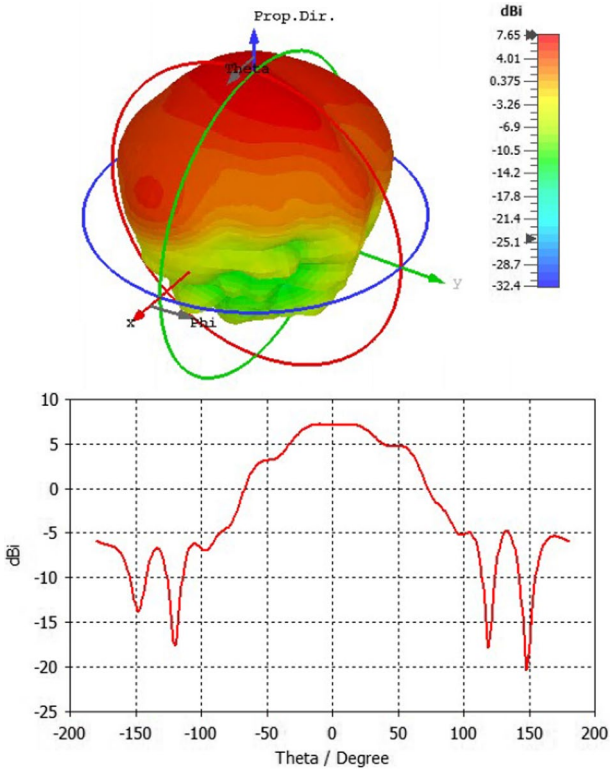

Fig. 7 The 3D radiation pattern and antenna gain pattern at phi = 90°

aperture. However, from the perspective of the imaging performance, the higher resolution requires sufficient large aperture size of the antenna.

To solve this, we propose to use a sparse scanning approach to form even larger virtual aperture, which has been widely used in the field of remote sensing and monitoring in satellite-air-based platforms [14]. With this technique, the echo signals are collected at different times and different spatial locations with the moving of the imaging platform, and then they are combined in well-order into a virtual aperture that is much larger than the physical antenna size, thus achieving a better resolution.

One challenge brought by the virtual aperture imaging is that when a customer holds the device to perform imaging on an object, the scanning trajectory is irregular [15]. As a result, the collected echo signals is sparse. For example, the customer holds a smartphone mounted with imaging module to image an object with Z-shaped scanning trajectory, as shown in Fig. 8.

It can be found that the echo samplings in the horizontal direction are continuous, i.e., the spatial spacing between sampling points is comparable to the wavelength of the echo signal. However, this feature cannot be maintained in the vertical direction, since it is difficult for an untrained customer to keep the spacing between two adjacent lines of the scanning track in wavelength order. Therefore, the echo samplings in the vertical direction are sparse, which will cause strong side-lobe interference, and then result in artifacts. In serious cases, the target can't even be imaged.

To solve this challenge, we consider decomposing the scanning trajectory on a two dimensional (2D) plane into several sets of linear scanning tracks along the horizontal

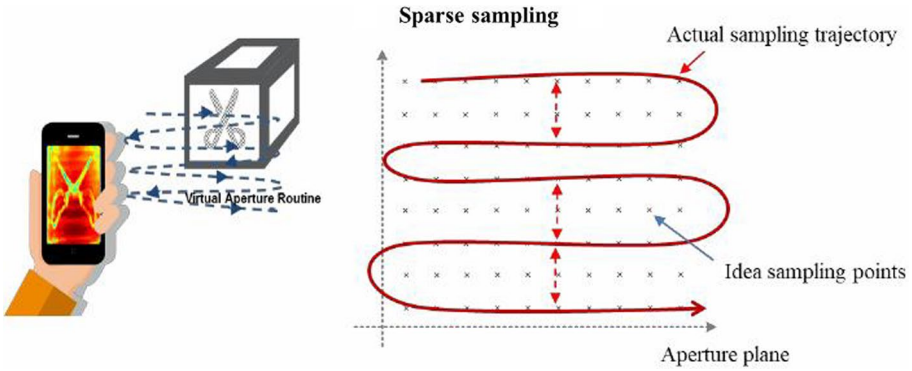

Fig. 8 Illustration of the irregular scanning trajectory of portable devices

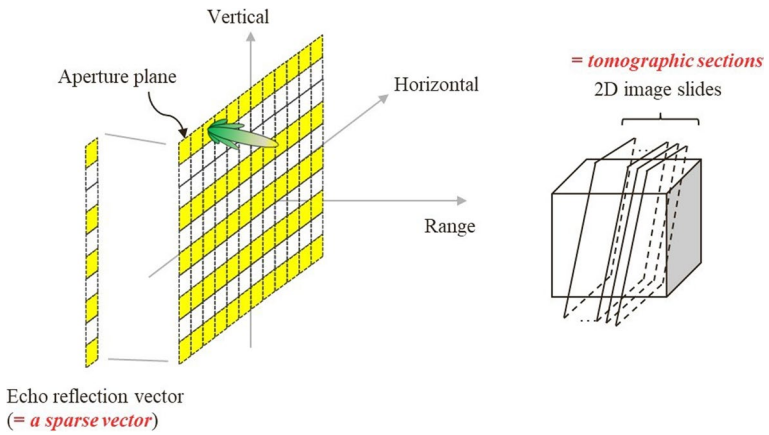

Fig. 9 Illustration of the sparse scanning approach and the tomographic imaging techniques

direction, where the sparseness of the sampling signals in the vertical domain is then equivalent to the sparseness between horizontal tracks, as illustrated in Fig. 9. In this case, the reflected information from the object can be retrieved from these vertically sparse samplings via compressed sensing techniques. After that, by using the concept of tomographic imaging, the echoed samplings obtained from each horizontal linear scanning track are imaged, and combined to form the final 3D image. Examples with different levels of vertical sparsity are shown.

3.3 Waveform evaluation

RF imaging has many different characteristics from optical image, making it complicated to assess the quality with unified metrics [16]. Also, the metrics to evaluate the selection of waveform for RF imaging are very different from that for communications where block error rate (BLER), throughput, and peak-to-average power ratio (PAPR) are the key performance indicators. Instead, for the performance evaluation of RF imaging at THz band, sensing accuracy and resolution are usually considered as key performance indicators. Furthermore, ambiguity functions (AF) and point spread functions (PSF) are treated as important metrics for waveform evaluation as well [16].

In the simulation for waveform evaluation, we consider an ISAC system at a portable device with a total bandwidth of 8 GHz operating at the carrier frequency of 140 GHz. Moreover, it is assumed that the portable device is equipped with one mono-static full duplex sensing antenna transmitting joint ISAC signal to a target nearby. For simplicity, we assume a point target with single line-of-sight channel [17]. And an ideal scanning trajectory with half wavelength spacing in both horizontal and vertical directions are applied in the simulation (i.e. no sparsity). Also we add an interference of 80 dB at the receiver to emulate the impact of full duplex working mode for both OFDM and frequency-modulated continuous wave (FMCW) waveforms. Phase noise is ignored due to small SNR degradation for mono-static sensing [18]. Other simulation configurations are listed in Table 1.

The PSF for both the range and cross-range are simulated to calculate the peak side-lobe ratio (PSLR) and integrated side-lobe ratio (ISLR) [19] for comparison. Figure 10 shows the results of the range and cross-range point spread function (PSF) for both OFDM and FMCW waveforms. The comparison of resolutions is further summarized in Table 2.

The simulation results show that FMCW and OFDM have similar cross-range performance. Though OFDM has slightly better range ISLR, it has worse range resolution. Considering that various performance requirements of sensing applications, we hope that the above simulations can help to select alternative waveforms for THz imaging applications. For long range communication in the uplink, OFDM is not favorable due to its high PAPR, but for THz imaging applications on portable devices, where the typical sensing range is within tens of meters, both of these two waveforms could be considered as potential candidates.

4 Implementation

The prototype is tested with a robotic arm imitating trajectory of human hand. A metal lemon core in Fig. 11a, with a diameter of 8 cm, is placed on top of the 4 cm tall foam and is 50 cm from the sensing device for better demonstation. Even though we use only metal target here, target of diferent kinds of materials can also be used for imaging. Besides, the absorbing material is placed beneath the foam.

Table 1 Simulation configurations

Parameter	OFDM	FMCW
Carrier frequency (GHz)	140	140
Bandwidth (GHz)	8	8
Frequency sampling (GHz)	9.8304	0.0128
Distance (m)	1	1
Virtual array	128*128	128*128
SNR (dB)	− 21.4	− 21.4
Target RCS (m^2)	0.01	0.01
CP (ns)	59	–
FFT size	8192	1024
Tp (us)	–	50

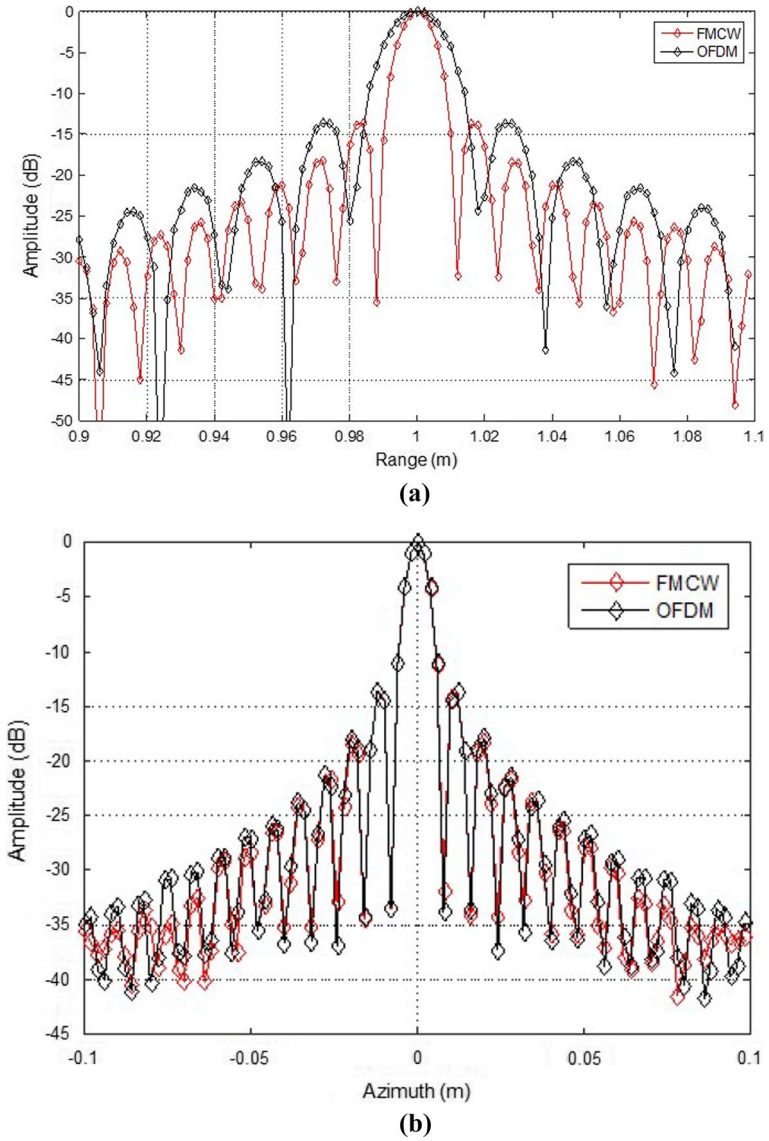

Fig. 10 Comparison of FMCW and OFDM waveforms. **a** Range PSF. **b** Cross-range PSF

Table 2 Waveform simulation results

Waveform	PSLR (dB)		ISLR (dB)		Resolution (m)	
	Range	Cross-range	Range	Cross-range	Range	Cross-range
FMCW	− 13.6	− 13.8	− 10.5	− 10.3	0.012	0.008
OFDM	− 13.66	− 13.75	− 11.0	− 10.2	0.015	0.008

As depicted in Fig. 11b, the robotic arm scans at a speed of 1 m/s with the scanning area set as 10 cm by 12 cm in the prototype. The longitudinal spacing of the scan trajectories are controlled to simulate the sparsity in the trajectories of the user's hand-held scan behavior. The spatial position information from the robotic arm and

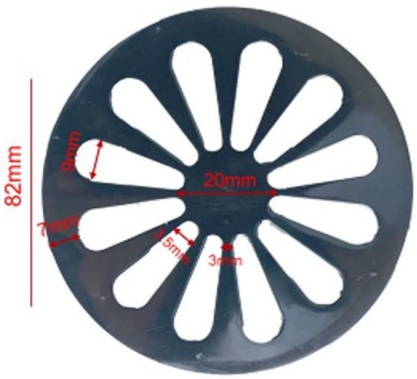

(a)

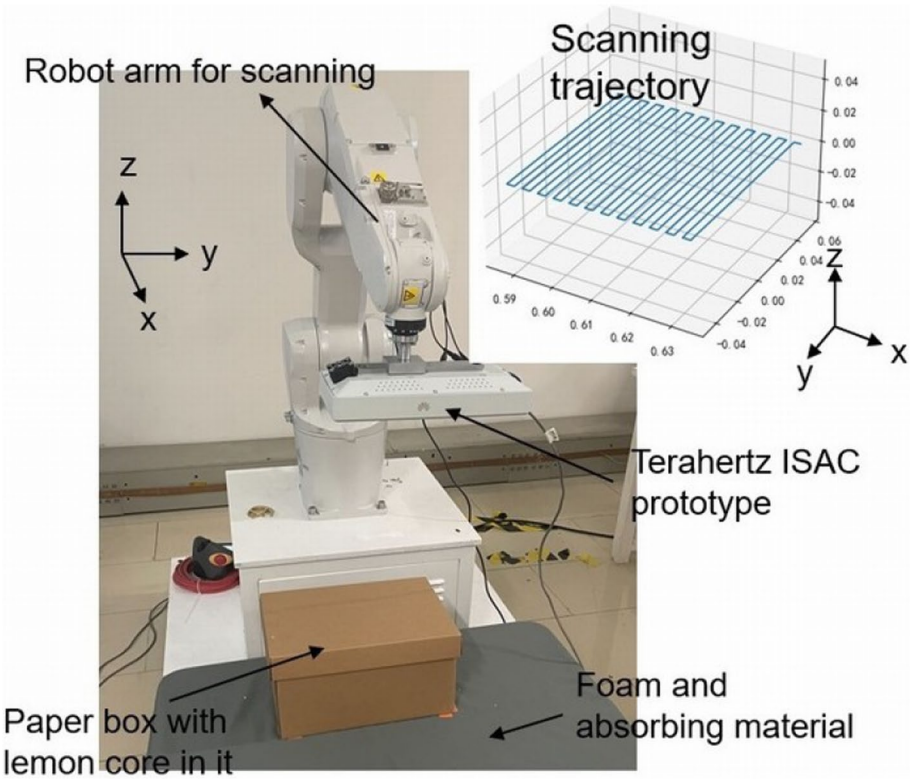

(b)

Fig. 11 Implementation setup. **a** A metal lemon core for image. **b** Measurement setup for THz sensing on portable devices

the MEMS are feedback simultaneously, and synchronized with the received echo signals. Here, the position information from robot arm is used to correct the information from the MEMS. In this paper, the scanning path in the test apply the regular scanning as shown in Fig. 11, which takes about 40 s. The position returned by the MEMS will then be used for sparse free hand scanning imaging enhanced by the 4T16R to reduce the scan path, which would achieve less than 10 s scanning time.

5 Methods

The single-input single-output (SISO) imaging method used in this paper is the traditional methods including backprojection algorithm [20] and tomography algorithm [21]. This paper mainly focuses on the single-input multiple-output (SIMO) imaging method.

Multiple receivers can greatly reduce the imaging time and improve the imaging quality compared with one receiver. Theoretically, n receivers can reduce the sampling time to $1/n$ compared with one receiver under the same imaging quality. Less sampling time will reduces the difficulty of motion error compensation, which will improve the imaging quality in return. However, the gains and time delays of different receiver channels are difficult to be consistent due to factors such as RX channel hardware, antenna position, platform attitude and equipment noise. Multichannel amplitude and phase imbalance leads to azimuth ghosting, which will significantly affect the imaging quality. Since the amplitude error can be easily compensated by multichannel amplitude equalization methods [22, 23], this paper mainly focus on back projection algorithm with a noval multichannel phase error compensation method.

The whole multichannel imaging process based on back projection algorithm can be viewed as time-domain coherent integration of electromagnetic signals from multiple receivers. Let the vector $\boldsymbol{b}_k$ denote the filtered backprojection of pulse k over all pixels of interest. The nth channel (vectorized) image is computed as

$$\boldsymbol{z}_n = \sum_k \boldsymbol{b}_k. \tag{1}$$

When the single-channel image are subject to phase errors, the objective of the multichannel phase compensation algorithm is to produce phase estimates $\hat{\boldsymbol{\theta}} = \{\hat{\theta}_1, \hat{\theta}_2 \ \ldots, \hat{\theta}_N\}$ such that the multichannel image quality of

$$z = \sum_n \boldsymbol{z}_n e^{-j\hat{\theta}_n}. \tag{2}$$

is maximized over a given metric. As motivated by image sharpness maximization criterion, we consider the sharpness metric $s(\hat{\theta}) = \sum_i v_i^2$, where v_i is the magnitude of the ith pixel. Therefore, the optimal correction is

$$\hat{\theta} = \arg\max_{\theta} s(\theta). \tag{3}$$

Since the optimization in (3) has no closed-form solution, this paper resort to an $(N-1)$ step method. We set the 1st channel as the reference channel, then the phase estimates can be simplified as $\hat{\boldsymbol{\theta}} = \{0, \hat{\theta}_1 \ \ldots, \hat{\theta}_{N-1}\}$. Let $\hat{\theta}_i$ denote the ith channel phase correction of the ith step; then, the phase error estimation at the next step $i+1$ is defined as

$$\hat{\theta}_{i+1} = \arg\max_{\theta} s(0, \hat{\theta}_1, \ldots, \hat{\theta}_i, \theta) \tag{4}$$

When holding the previous channels' phases constant, the reflectivity image $\boldsymbol{z}(\phi)$ at ith step can be defined as

$$\boldsymbol{z}(\theta) = \sum_{i=1}^{i} e^{-j\hat{\theta}_{i-1}} \hat{\boldsymbol{b}}_p + e^{-j\theta} \hat{\boldsymbol{b}}_i \tag{5}$$

$$= \boldsymbol{x} + e^{-j\theta} \boldsymbol{y} \tag{6}$$

where $\boldsymbol{x}$ comprises the backprojection sum of all pulses from $1 \sim i-1$ channel except for pulses from ith channel and $\boldsymbol{y}$ is the uncorrected phase of ith channel. The associated intensity of the mth pixel of $z(\theta)$ is

$$v_m = z_m z_m^* = (x_m + e^{-j\theta} y_m)(x_m^* + e^{j\theta} y_m^*) \tag{7}$$

$$= |x_m|^2 + |y_m|^2 + 2\Re(e^{j\theta} y_m^*) \tag{8}$$

As we can see, $(\boldsymbol{v}_0)_m = |x_m|^2 + |y_m|^2$ is constant and $(\boldsymbol{v}_\theta)_m = 2\Re(e^{j\theta} y_m^*)$ depends on the unknown phase of the pulses from ith channel. The sharpness of the image is

$$\sum_m v_m^2 = \|v\|^2 \tag{9}$$

Therefore, the optimal phase correction for the pulses from ith channel is the value of θ that maximizes the squared length of v.

If we define the vectors $\boldsymbol{p}$ and $\boldsymbol{q}$ with elements $p_m = 2\Re(y_m^* x_m e^{j\theta})$ and $b_m = -2\Im(y_m^* x_m)$, $\boldsymbol{v}_\theta$ may be written as

$$\boldsymbol{v}_\theta = \boldsymbol{p}\cos\theta + \boldsymbol{q}\sin\theta. \tag{10}$$

which is an interpretation of an ellipse in in a geometric sense. The displacement vector$\boldsymbol{v_0}$ can be decomposed into a portion in the $\boldsymbol{p}$ and $\boldsymbol{q}$. In this paper, we choose an orthonormalization of $\boldsymbol{p}, \boldsymbol{q}$ to represent the basis $\{\boldsymbol{s}_1, \boldsymbol{s}_2\}$ for convenience

$$\boldsymbol{s_1} = \frac{\boldsymbol{p}}{\|\boldsymbol{p}\|} \quad \boldsymbol{s_2} = \frac{\boldsymbol{q} - \boldsymbol{s_1}\boldsymbol{s_1}^T\boldsymbol{q}}{\left\|\boldsymbol{q} - \boldsymbol{s_1}\boldsymbol{s_1}^T\boldsymbol{q}\right\|} \tag{11}$$

We got a new coordinate system

$$\hat{\boldsymbol{p}} \equiv \begin{bmatrix} \hat{p}_1 \\ \hat{p}_2 \end{bmatrix} = \boldsymbol{S}^T\boldsymbol{p} \quad \hat{\boldsymbol{q}} \equiv \begin{bmatrix} \hat{q}_1 \\ \hat{q}_2 \end{bmatrix} = \boldsymbol{S}^T\boldsymbol{q} \tag{12}$$

where $\boldsymbol{S} = [s1\ s2]$. After projected onto the new coordinate system, the point becomes

$$\boldsymbol{x}_0 = \boldsymbol{E}^T(\boldsymbol{E}\boldsymbol{E}^T)(-\boldsymbol{v_0}) = -\boldsymbol{E}^T\boldsymbol{v_0}. \tag{13}$$

Finally, the optimization problem is transformed into a geometry problem. We has to find the point $\hat{\boldsymbol{x}}$ on the ellipse lying farthest form the given point $\boldsymbol{x}_0$. The unclosed form solution problem for the optimal phase correction becomes a closed-form solution problem after the geometry interpretation. The solution method is similar to [24]. If $\hat{\boldsymbol{x}}$ is the farthest point, the vector $\boldsymbol{x}_0 - \hat{\boldsymbol{x}}$ will be parallel to the normal $e(\boldsymbol{x})$ of the ellipse

$$\boldsymbol{x}_0 - \hat{\boldsymbol{x}} = \beta e(\hat{\boldsymbol{x}}) \tag{14}$$

where β is a real constant. The ellipse may be written $\boldsymbol{x}(\theta) = [x_1\ x_2]^T = \hat{\boldsymbol{p}}\cos\theta + \hat{\boldsymbol{q}}\sin\theta$ or implicitly

$$f(\boldsymbol{x}) = \boldsymbol{x}^T \boldsymbol{O}\boldsymbol{x} = 1 \tag{15}$$

with

$$\boldsymbol{O} = \begin{bmatrix} o_1 & o_3 \\ o_3 & o_2 \end{bmatrix} \tag{16}$$

where

$$o_1 = (\hat{p}_2^2 + \hat{q}_2^2)/r \tag{17}$$

$$o_2 = (\hat{p}_1^2 + \hat{q}_1^2)/r \tag{18}$$

$$o_3 = -(\hat{p}_1\hat{p}_1 + \hat{q}_1\hat{q}_2)/r \tag{19}$$

$$r = (\hat{p}_2\hat{q}_1 - \hat{p}_1\hat{q}_2)^2 \tag{20}$$

Hence, the normal $e(\boldsymbol{x})$ may be computed by gradient for $f(\boldsymbol{x})$

$$e(\boldsymbol{x}) \equiv \nabla f((x)) = 2\boldsymbol{O}\boldsymbol{x}. \tag{21}$$

The $\hat{\boldsymbol{x}}$ can be written as

$$\hat{\boldsymbol{x}} = (\beta\boldsymbol{O} + \boldsymbol{I})\boldsymbol{V}^T \tag{22}$$

The eigendecomposition of $\boldsymbol{O}$ is

$$\boldsymbol{O} = \boldsymbol{V}\boldsymbol{\Lambda}\boldsymbol{V}^T. \tag{23}$$

Substituting Eqs. (23) and (22) into (15), we can obtain

$$1 = \boldsymbol{x}_0(\beta\boldsymbol{O} + \boldsymbol{I})\boldsymbol{O}(\beta\boldsymbol{O} + \boldsymbol{I})^{-1}\boldsymbol{x}_0 \tag{24}$$

$$= \boldsymbol{x}_0^T\boldsymbol{V}(\beta\boldsymbol{\Lambda} + \boldsymbol{I})^{-1}\boldsymbol{\Lambda}(\beta\boldsymbol{\Lambda} + \boldsymbol{I})^{-1}\boldsymbol{\Lambda}^T\boldsymbol{x}_0 \tag{25}$$

$$= \boldsymbol{x}_0^T\boldsymbol{V}\begin{bmatrix} \frac{\lambda_1}{(\beta\lambda_1+1)^2} & 0 \\ 0 & \frac{\lambda_2}{(\beta\lambda_2+1)^2} \end{bmatrix}\boldsymbol{V}^T\boldsymbol{x}_0 \tag{26}$$

where λ_1 and λ_2 represent the eigenvalues of $\boldsymbol{O}$.

Letting $[\gamma_1\ \gamma_2]^T = \boldsymbol{V}^T\boldsymbol{x}_0$, the Eq. (26) becomes

$$\gamma_1^2\frac{\lambda_1}{(\beta\lambda_1 + 1)^2} + \gamma_2^2\frac{\lambda_2}{(\beta\lambda_2 + 1)^2} - 1 = 0. \tag{27}$$

The Eq. (27) has the same roots as

$$\sum_{i}^{4} \delta_i \beta^i = 0 \tag{28}$$

where

$$\delta_0 = \lambda_1 \gamma_1^2 + \lambda_2 \gamma_2^2 - 1 \tag{29}$$

$$\delta_1 = 2\lambda_1(\lambda_2 \gamma_2^2 - 1) + 2\lambda_2(\lambda_1 \gamma_1^2 - 1) \tag{30}$$

$$\delta_2 = (\lambda_1 \gamma_1^2 - 1)\lambda_2^2 + (\lambda_2 \gamma_2^2 - 1)\lambda_1^2 - 4\lambda_1 \lambda_2 \tag{31}$$

$$\delta_3 = -2\lambda_1 \lambda_2 (\lambda_1 + \lambda_2) \tag{32}$$

$$\delta_4 = -(\lambda_1 \lambda_2)^2. \tag{33}$$

There are up to four real roots in Eq. (28). The smallest real root represents the farthest point on the ellipse [24]. Let $\hat{\beta}$ denote the smallest real root of Eq. (28); then we have

$$\begin{bmatrix} \cos\hat{\beta} \\ \sin\hat{\beta} \end{bmatrix} = [\hat{\boldsymbol{p}}\ \hat{\boldsymbol{q}}]^{-1}(\hat{\beta}\boldsymbol{O} + \boldsymbol{I})^{-1}\boldsymbol{x}_0. \tag{34}$$

The optimal phase correction $\hat{\beta}$ may be written as

$$\hat{\beta} = \tan^{-1}\left(\frac{\sin\hat{\beta}}{\cos\hat{\beta}}\right) \tag{35}$$

6 Result and discussion

6.1 SISO imaging

Based on the testbed setup shown in Fig. 11, the proof-of-concept THz imaging performance with different sparsity configurations in the scanning patterns are presented and compared through Figs. 12, 13 and 14 below.

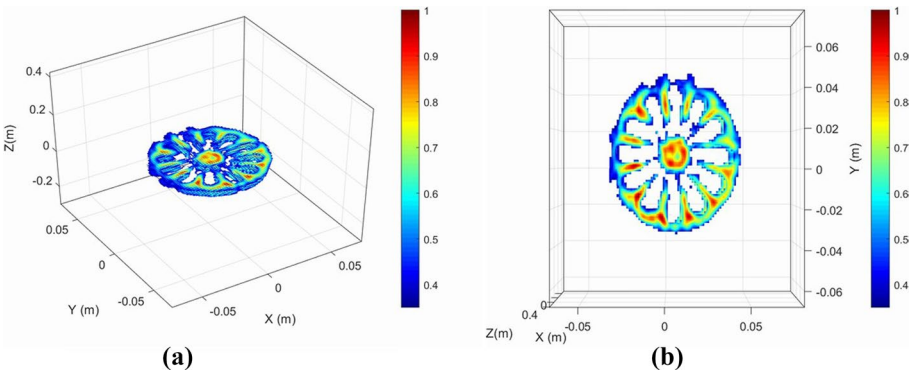

Fig. 12 The imaging results of non-sparse full aperture scanning. **a** Three-dimentional image. **b** Cross-range profile (Top-down view)

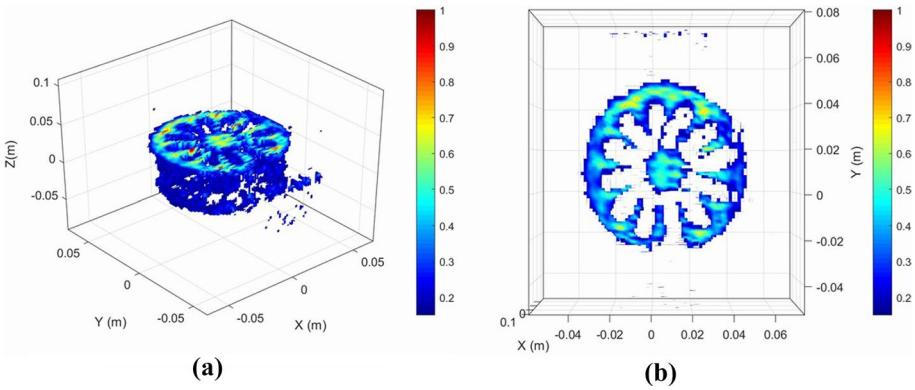

Fig. 13 The imaging results of sparse scanning with 50% sparsity. **a** Three-dimentional image. **b** Cross-range profile (Top-down view)

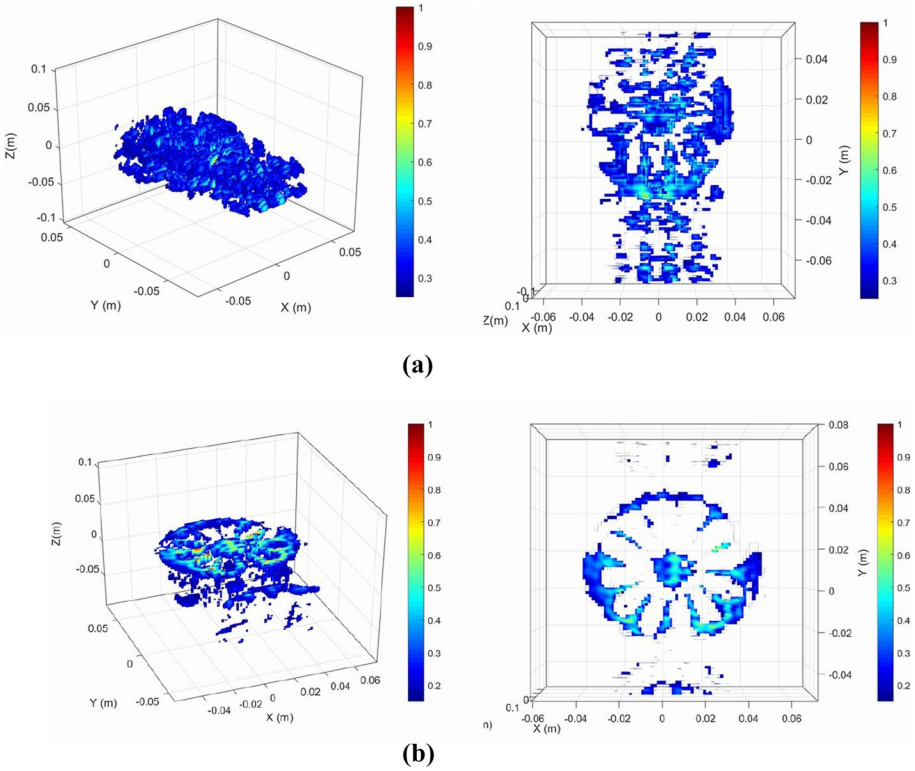

Fig. 14 The imaging results of sparse apeture scanning with 75% sparsity. Left: three-dimentional image; Right: cross-range profile (Top-down view). **a** Imaging with traditional tomography approach [25]. **b** Imaging with compressive sensing based tomography approach

Firstly, in Fig. 12, non-sparse full aperture scanning is assumed, in which the vertical sampling is non-sparse, thus achieving the best PSLR and ISLR. This mode is set up as an upper bound performance reference. Then, in order to simulate the sparsity in free hand scanning to further reduce the scan time, we assume various sparsity in test. Measurements with sparse scanning, in which the sampling in vertical is sparse, are evaluated and presented in Figs. 13 and 14 for 50% and 75% sparsity, respectively. Here 50% and

75% sparsity mean that there are 50% and 25% non-zero samplings in the vertical direction, respectively. These modes are set up to simulate the behavior of scanning with a handheld device in real world case. Note that the higher the sparsity, the less the collected sampling and thus the stronger the side-lobe interference occurred at the resulted aperture, representing a worse scanning condition.

From these measured results above, it can be concluded that the objects can be well imaged (i.e. the outline of the metal lemon core can be clearly outlined) with limited loss even with 75% sparsity if advanced algorithms are applied. This implies that the millimeter-level resolution of image can be achieved by the prototype THz ISAC system. Furthermore, it is also observed that, more artifacts occur in the image as the sparsity of the scanning trajectory increases. This phenomenon is due to the side-lobe interference of irregular echo sampling mentioned. Such interference would cause destructive impact if no advanced signal processing algorithm is applied.

6.2 SIMO imaging

SIMO imaging results based on backprojection without phase error compensation Fig. 15a, with salient point method Fig. 15b and with the geometric interpretation algorithm Fig. 15c are shown in Fig. 15.

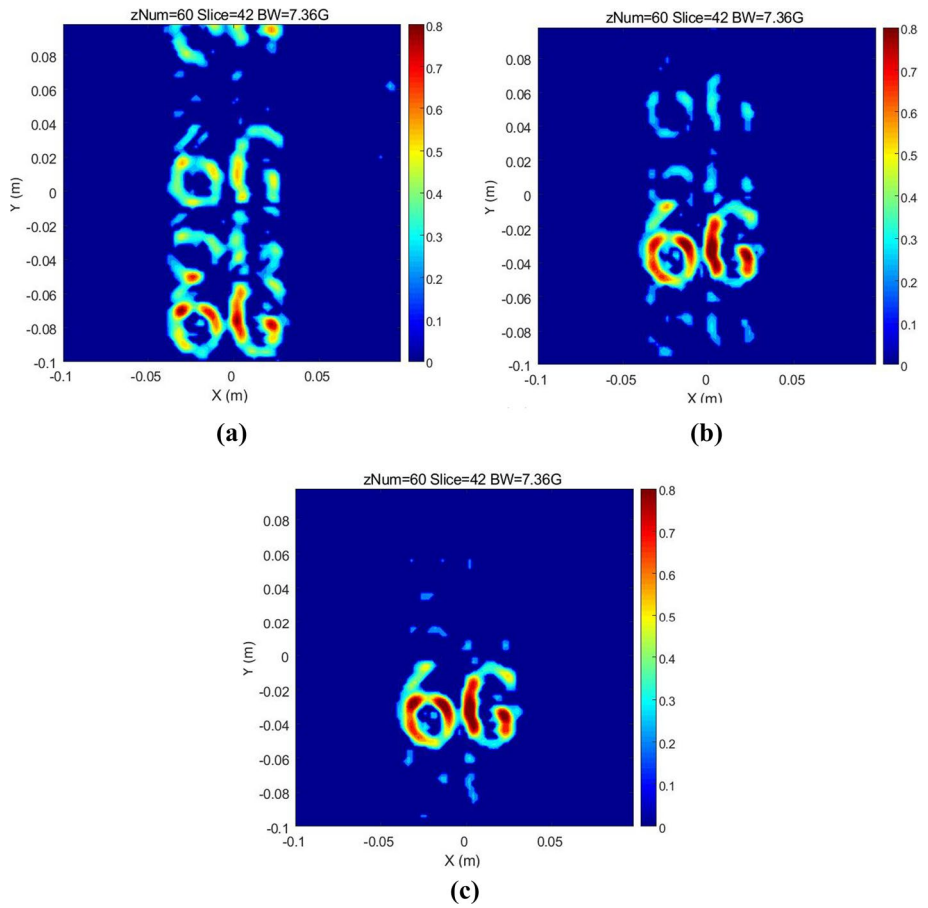

Fig. 15 SIMO imaging results. **a** Backprojection without phase error compensation. **b** Backprojection with salient point method. **c** Backprojection with the geometric interpretation algorithm

In SIMO imaging scenerio, the scan time can be reduced to $1/n$ theoretically with n receive channels compared with the scan time of SISO imaging. In our experiment, the SIMO imaging scan time is 10.2 s. Data processing can be performed simultaneously with imaging scans. The whole time from data acquisition to imaging results is 12.4 s. The experiments are conducted on a laptop computer with i7-8550U (1.8 GHz) and 16 GB memory. We can greatly shorten the time with MIMO down to less than 2 s within the next 6 months. We believe the near-real-time applications can be implemented.

As a summary, we can conclude that with the proposed virtual aperture solution and advanced signal processing algorithms, mm-level imaging resolution is achievable on a portable device working in hand-held scanning mode.

7 Conclusion

In this paper, we discussed the advantages and application scenarios of THz sensing and in particular, we demonstrated with a THz prototype that by applying the proposed virtual aperture solution, THz sensing on a portable device can achieve millimeter level sensing accuracy. The proposed virtual aperture solution has been implemented at 140 GHz with 8 GHz bandwidth and a 4T16R MIMO structure in the hardware architecture and a sparse scanning approach that exploited time and spatial degree-of-freedom to further extend the size of the virtual aperture. Different waveforms and different levels of sparsity have been evaluated and compared, verifying the feasibility of using THz communication signals to achieve mm-level sensing resolution.

Abbreviations

THz	Terahertz
ISAC	Integrated sensing and communication
AI	Artificial intelligence
WRC	World radiocommunication conference
MS	Mobile service
LIDAR	Light detection and ranging
CT	Computed tomography
MIMO	Multiple-input multiple-output
KPI	Key performance indicator
OFDM	Orthogonal frequency division multiplexing
LFM	Linear frequency modulation
RF	Radio frequency
PLL	Phase-locked loop
MEMS	Micro-electro-mechanical systems
EIRP	Equivalent isotropically radiated power
QAM	Quadrature amplitude modulation
2D	Two dimensional
3D	Three dimensional
BLR	Block error rate
PAPR	Peak-to-average power rate
AF	Ambiguity functions
PSF	Point spread functions
FMCW	Frequency modulated continuous wave
SNR	Signal-to-noise ratio
PSLR	Peak side-lobe ratio
ISLR	Integrated side-lobe ratio
SISO	Single-input single-output
SIMO	Single-input multiple-output

Acknowledgements

The authors would like to thank the anonymous reviewers for their valuable comments and suggestions that helped to improve the quality of this manuscript.

Author Contributions

All authors have contributed equally. All authors have read and approved the manuscript.

Availability of data and materials
Not available on line. Please contact the author for data requests.

Declarations

Competing interests
The authors declare that they have no competing interests.

Received: 18 October 2021 Accepted: 1 September 2022
Published online: 22 October 2022

References

1. W. Tong, P. Zhu, *6G, the Next Horizon: From Connected People and Things to Connected Intelligence* (Cambridge University Press, Ottawa, 2021)
2. A.F. Martone, K.A. Gallagher, K.D. Sherbondy, Joint radar and communication system optimization for spectrum sharing, in *2019 IEEE Radar Conference (RadarConf)* (IEEE, 2019), pp. 1–6
3. T. Kürner, Turning thz communications into reality: status on technology, standardization and regulation, in *2018 43rd International Conference on Infrared, Millimeter, and Terahertz Waves (IRMMW-THz)* (IEEE, 2018), pp. 1–3
4. H. Zhan, Q. Li, K. Zhao, L. Zhang, Z. Zhang, C. Zhang, L. Xiao, Evaluating pm2. 5 at a construction site using terahertz radiation. IEEE Trans. Terahertz Sci. Technol. **5**(6), 1028–1034 (2015)
5. S. Nakajima, H. Hoshina, M. Yamashita, C. Otani, N. Miyoshi, Terahertz imaging diagnostics of cancer tissues with a chemometrics technique. Appl. Phys. Lett. **90**(4), 041102 (2007)
6. D. Nüßler, J. Jonuscheit, Terahertz based non-destructive testing (NDT). tm-Technisches Messen **88**(4), 199–210 (2021)
7. S. Hu, C. Shu, Y. Alfadhl, X. Chen, Advanced thz mimo sparse imaging scheme using multipass synthetic aperture focusing and low-rank matrix completion techniques. IEEE Trans. Microw. Theory Tech. **70**(1), 659–669 (2021)
8. A.R. Chiriyath, B. Paul, G.M. Jacyna, D.W. Bliss, Inner bounds on performance of radar and communications coexistence. IEEE Trans. Signal Process. **64**(2), 464–474 (2015)
9. Z. Feng, Z. Fang, Z. Wei, X. Chen, Z. Quan, D. Ji, Joint radar and communication: a survey. China Commun. **17**(1), 1–27 (2020)
10. C.B. Barneto, T. Riihonen, M. Turunen, L. Anttila, M. Fleischer, K. Stadius, J. Ryynänen, M. Valkama, Full-duplex ofdm radar with lte and 5g nr waveforms: challenges, solutions, and measurements. IEEE Trans. Microw. Theory Tech. **67**(10), 4042–4054 (2019)
11. K. Siddiq, R.J. Watson, S.R. Pennock, P. Avery, R. Poulton, B. Dakin-Norris, Phase noise analysis in fmcw radar systems, in *2015 European Microwave Conference (EuMC)* (IEEE, 2015), pp. 1523–1526
12. P. Kumari, S.A. Vorobyov, R.W. Heath, Adaptive virtual waveform design for millimeter-wave joint communication-radar. IEEE Trans. Signal Process. **68**, 715–730 (2019)
13. Y. Gao, M.T. Ghasr, R. Zoughi, Effects of translational position error on microwave synthetic aperture radar (sar) imaging systems, in *2018 IEEE International Instrumentation and Measurement Technology Conference (I2MTC)* (IEEE, 2018), pp. 1–6
14. J.T. Case, M.T. Ghasr, R. Zoughi, Nonuniform manual scanning for rapid microwave nondestructive evaluation imaging. IEEE Trans. Instrum. Meas. **62**(5), 1250–1258 (2012)
15. G. Alvarez-Narciandi, M. Lopez-Portugues, F. Las-Heras, J. Laviada, Freehand, agile, and high-resolution imaging with compact mm-wave radar. IEEE Access **7**, 95516–95526 (2019)
16. A.A. Tuzova, V.A. Pavlov, A.A., Belov, S.V. Volvenko, Comparison of image quality assessment metrics for evaluation of performance of anisotropic diffusion filter for sar images, in *2020 IEEE International Conference on Electrical Engineering and Photonics (EExPolytech)* (IEEE, 2020), pp. 176–179
17. P. Kumari, J. Choi, N. González-Prelcic, R.W. Heath, IEEE 802.11 ad-based radar: an approach to joint vehicular communication-radar system. IEEE Trans. Veh. Technol. **67**(4), 3012–3027 (2017)
18. A. Dürr, B. Schweizer, J. Bechter, C. Waldschmidt, Phase noise mitigation for multistatic fmcw radar sensor networks using carrier transmission. IEEE Microw. Wirel. Compon. Lett. **28**(12), 1143–1145 (2018)
19. K. Farnane, K., Minaoui, A. Rouijel, D. Aboutajdine, Analysis of the ambiguity function for phase-coded waveforms, in *2015 IEEE/ACS 12th International Conference of Computer Systems and Applications (AICCSA)* (IEEE, 2015), pp. 1–4
20. A.F. Yegulalp, Fast backprojection algorithm for synthetic aperture radar, in *Proceedings of the 1999 IEEE Radar Conference. Radar Into the Next Millennium (Cat. No. 99CH36249)* (IEEE, 1999), pp. 60–65
21. K. Knaell, G. Cardillo, Radar tomography for the generation of three-dimensional images. IEE Proc. Radar Sonar Navig. **142**(2), 54–60 (1995)
22. J.E.A. Moreira, X-sar interferometry: first results. IEEE Trans. Geosci. Remote Sens. **33**(4), 950–956 (1995)
23. T. Jin, X. Qiu, D. Hu, C. Ding, Unambiguous imaging of static scenes and moving targets with the first Chinese dual-channel spaceborne sar sensor. Sensors **17**(8), 1709 (2017)
24. J.C. Hart, *Distance to an Ellipsoid. Graphics Gems* (Academic Press, Boston, 1994)
25. A. Vertiy, S. Gavrilov, Near-field millimeter wave and microwave tomography imaging, in *2007 International Kharkov Symposium Physics and Engineering of Millimeter and Sub-Millimeter Waves (MSMW)*, vol. 1 (IEEE, 2007), pp. 104–108

Publisher's Note